Article

Mechanical Properties of a 3D Printed Wall Segment made with an Earthen Mixture

Elena Ferretti [1],*, Massimo Moretti [2], Alberto Chiusoli [2], Lapo Naldoni [2], Francesco De Fabritiis [2] and Massimo Visonà [2]

[1] Department of Civil, Environmental and Materials Engineering—DICAM, Alma Mater Studiorum Università di Bologna, Viale del Risorgimento 2, 40136 Bologna (BO), Italy; elena.ferretti2@unibo.it
[2] WASP s.r.l., Via Castelletto 104/106, 48024 Massa Lombarda (RA), Italy; alberto@3dwasp.com
* Correspondence: elena.ferretti2@unibo.it; Tel.: +39-051-209-35-15

Abstract: This study provides a contribution to the research field of 3D printed earthen buildings, focusing, for the first time, on the load-bearing capacity of these structures. The study involves the entire production and testing process of the earthen elements, from design, to the preparation of the mixture and the 3D printing, up to the uniaxial compression test on a wall segment. The results indicate that 3D printed earthen elements have a compressive strength of 2.32 MPa, comparable to that of rammed earth structures. The experimental data also made it possible to draw conclusions on the action of the infill, which seems to have the function of stopping the propagation of cracks. This has a positive effect on the overall behavior of 3D printed earthen elements, since it avoids the onset of dilative behavior in the final stages of the load test and maintains ultimate load values higher than 50% of the maximum load.

Keywords: 3D printing; earthen buildings; bio-composites; load-bearing walls; orthotropic material; crack propagation; Poisson’s ratio; volumetric strain; mesoscale behavior; microscale behavior

1 Introduction

Earthen construction (i.e. the construction of structural units manufactured from soil) is one of the oldest and most widespread vernacular building techniques. Over the centuries, it gave rise to three main traditional construction techniques: adobe (or compressed earth blocks), rammed earth and cob.

The advent of industrialization has progressively supplanted the earthen construction techniques, considered expressions of building in poverty conditions, overtaken by progress and well-being. Recently, however, earthen construction has regained a lot of attention in the construction sector, due to its low environmental impact and its recyclability [1–4]. In fact, earthen structures need a fraction of the energy required to manufacture and process an equivalent amount of fired bricks or concrete (low embodied energy) [5–7], require lower carbon emissions for construction (low carbon footprint) [8] and consume less operational energy than conventional structures (high energy efficiency) [9]. Finally, earthen materials also need less energy to recycle them [10]. Nevertheless, the cost of labor, the time it takes for the material to harden and a slower production rate than in the concrete industry result in high finished product costs, which limited the development of earthen construction in modern times [11]. The problem of slowness in production is particularly problematic to solve, since fast production usually does not allow achieving sufficient strength in the dry state. Therefore, the primary concern in setting up a mix design for an earthen mixture is to provide a viable solution to both the production rate problem and the dry state strength problem.

Among the recently introduced unconventional methods to improve construction speed with earth [12–15], digital-based construction methods, such as 3D printing, are particularly promising. As with extrusion-based additive manufacturing methods for concrete [16,17], the quality of the 3D printing process for earthen materials is the result of a trade-off between two competing requirements: material deposition speed and construction speed. This means that the setting of the material must begin as soon as possible, so that the deposited material can withstand the increasing load induced by the subsequently deposited layers. Since the material must also have high strengths in the hardened (dry) state [18,19], the 3D printing process of earthen materials should integrate the research line on soil stabilization. In fact, this line of research – originally created for traditional earthen structures [20] – boasts many years of study on techniques suitable for improving the mechanical properties of earthen structures in the hardened state. This led, for example, to investigate the role of different stabilizers in the preparation of Compressed Stabilized Earth Blocks (CSEBs) [21–23] and to identify the optimum use of stabilizers [24–27] also in order to meet the criteria of the local building code [28].

From the point of view of the evolution of the soil stabilization techniques, soil stabilization first made use of stabilizers of natural origin – such as the addition of vegetable fibers [29,30] and biomaterial in the form of egg whites or proteins [31–33] – and, subsequently, of industrial stabilizers, such as lime [34] and Portland cement [35]. However, these remedies do not have the same impact on the environmental and are not all equally sustainable [36], an aspect that has become increasingly important with the recent development of sensitivity to environmental issues. Particularly detrimental to sustainability is the use of cement, as it leads to an increase in embodied energy, carbon footprint and operational energy and reduces the potential for recyclability [10,37–39]. This led to a renewed interest in bio-stabilization techniques, such as the use of microbial induced calcite precipitation (MICP) [40–42], different types of biopolymers (for example, xanthan gum [43–45], gellan gum [46], agar gum [46], guar gum [47], modified starch [47] and carrageenan [48]) and biopolymer additives [49], in both the construction [50] and geotechnical [51–54] sectors. Most of these techniques derive from the knowledge gained in the research on concrete. Just to give an example, in fact, the incorporation of bacteria in rice husk ash concrete increases the strength of concrete due to precipitation of calcium carbonate, which occurs at any age of the concrete [55,56].

One of the first companies to deal with 3D printing of earthen materials is the Italian WASP (acronym for World's Advanced Saving Project), which also developed a particular type of bio-composite for the stabilization of earthen mixtures [57]. WASP has also always been committed to the development of systems that allow the use of functional, end-use materials such as ceramics, porcelain, clay, and other advanced ceramics, in order to promote digital handicraft and self-production.

The WASP bio-composite is a combination of rice husk (RH) and lime. It exploits the high silica content of the RH and the time-delayed bio-cementation effect of the aerial lime, due to the carbonation of the lime [58]. Since carbonation continues indefinitely over time, the products of carbonation improve the mechanical properties of the earthen mixtures more and more over time [58], also protecting the vegetable fiber. In fact, the combination of a vegetable fiber with lime (a mineral) and water allows the vegetable fiber to mineralize and become resistant to bacteria, molds, insects, rodents and fire.

Since 2017, WASP undertook two different lines of research on earthen materials: the 3D printing of infill walls using natural mixtures of local origin without any type of chemical stabilization (Figure S1) and the 3D printing of load-bearing elements by additivating the mixtures with the minimum quantity of hydraulic lime-based stabilizers (Figure S2) [59]. The second line of research aims to create a new circular building model, entirely made with reusable and recyclable materials. The present work is part of this second line of research, which, of the two, is the richest in innovative aspects. Indeed, while it is quite common to find experimental results on earthen construction materials with organic compounds (even unusual) as stabilizers [60,61] and the 3D printing of earthen materials is becoming an increasingly interesting research topic [11,62,63], the mechanical characterization of 3D printed earthen elements for load-bearing use is still largely lacking in the scientific literature. To the authors' knowledge, this is actually the first scientific work dealing with the load-bearing capacities of 3D printed earthen elements with bio-stabilized soil.

Since one of the major problems in the view of load-bearing earthen walls is how to increase the number of floors of the earthen building (the load-bearing prototypes made so far are single-story), it is essential to investigate the failure mechanisms of earthen walls subjected to vertical loads. Of particular interest is to understand whether the individual extruded layers collaborate as a single body to withstand external loads. Another concern relates to the behavior of the outer shells at the time of the failure. Depending on the degree of cohesion with the internal infill, in fact, the outer shells may or may not undergo a wall overturning, moving by rigid motion independently of the rest of the wall. The experimental test presented in this work answers precisely these questions, never investigated until now.

One might regard this paper as the completion of a previous work on the study of the mechanical properties over time of bio-stabilized earthen mixtures [58], which is the equivalent for earthen materials of the description over time of the evolution of the cementitious materials [64–67], aimed at the rapid strength development in the material for 3D printing. The idea behind the experimental campaign discussed in [58] is to increase the cementing capacity of the RH-lime bio-composite by triturating the RH, which increases the contact surface between the RH and the earthen matrix. This favors the formation of Si-O-Si bonds and improves the mechanical properties of the earthen mixture. The results of [58] show that the stiffness values obtained with the shredded RH are actually higher than the stiffness values obtained with the non-shredded RH (all other conditions being equal, including the quantity of RH). Since this was precisely the expected result that motivated the experimentation of [58], the RH used in the wall segment of this paper (printed on the same day as the casting of the [58] specimens) is shredded RH.

2 Materials and Methods

To investigate the ability of 3D printed earthen walls to withstand the vertical loads, we tested an earthen wall segment with all the characteristic thicknesses in 1:1 scale. The dimensioning of the cross-section of the wall segment is in fact the typical one of the case studies in 1: 1 scale made by WASP, in the past (Figures S1, S2).

According to the Highway Research Board (HRB) [68]/UNI EN ISO 14688-1:2018 [69] soil classification, the soil collected on site for the preparation of the mixture is class A-4. This soil class has a wide distribution in Italy, with a greater presence in the Piedmont Po Plain of North-western Italy, in correspondence with large terraced alluvial fans, perched in the plains, connected with the middle-upper Pleistocene rivers of the Upper Piedmont [70]. The bio-stabilization of the A-4 soil took place using the RH-lime bio-composite, according to the principles described in [58]. Since the subject of this work is the load-bearing capacity of 3D printed earthen elements, for everything concerning the mechanical effect of the vegetable fiber on the properties of the hardened earthen mixture, we refer the reader to what we have already written in [58].

The test method chosen is the uniaxial compression test, conducted in the displacement control mode at the LiSG laboratory of the University of Bologna.

2.1 Mix Design and 3D Printing Process

The mix design of the earthen wall segment is one of the two used for the cubic specimens of [58], which shows the results of an experimental campaign on earthen mixtures with RH in two different grain sizes: unaltered RH for the TQ mix and shredded RH for the LT mix. The mix chosen for the wall segment of this paper is the LT mix (Table 1), with maximum size of the shredded RH equal to 2 mm. The specifications on the other components of the LT mix are in Table S1 of the supplementary material, to avoid repeating what already extensively described in [58].

Table 1. Percentage composition by weight of the LT mix.

Component	Percentage by weight
Soil	70.42%

Lime-based binder	4.70%
Hydraulic lime	4.69%
Shredded rice husk	1.41%
Silica sand	18.78%

The preparation of the mixture and the 3D printing of the specimen took place at the WASP headquarters (Massa Lombarda, Italy).

The 3D printed specimen of the experimental test is a parallelepiped with design dimensions of $730 \times 530 \times 504\, mm$ (length x depth x height). It consists of 42 extruded layers $12\, mm$ high. The print geometry includes two perimeter shells to confine the infill stratigraphy (Figure 1), which is consistent with the usual way of designing WASP 3D printed walls in case studies, since 2017. This geometric configuration with outer shells and infill is similar to that adopted in the Contour Crafting technique for concrete [71,72].

The infill is a regular mesh grid, characterized by double symmetry and orthogonality of the lines. Ten equidistant straight sections $35\, mm$ thick make up the infill, 5 with an inclination of $+45°$ and 5 with an inclination of $-45°$ (Figure 1). The distance between two successive intersections of the straight sections is approximately $150\, mm$.

To ensure a good grasp between infill and perimeter shells, the infill extends into the external cladding for $1/4$ of its total thickness (Figure 1), which is equal to $68\, mm$ (the two perimeter shells have a thickness of $34\, mm$ each). The partial interpenetration between infill and perimeter shells resulted in 10 vertical ribs along the outer perimeter of the specimen.

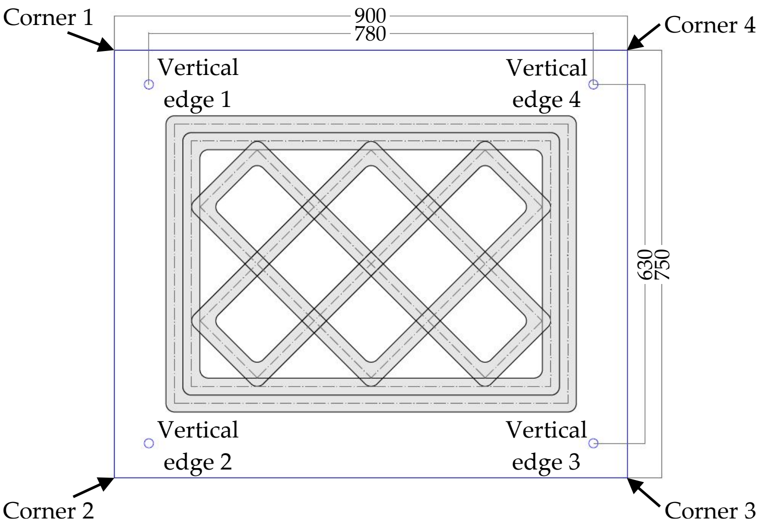

Figure 1. Dimensions of the specimen cross-section and of the $1{,}5\, cm$ thick load distribution plate.

Considering the curvature of the layers at the corners of the specimen, the gross area of the cross-section, A_g, is $374400\, mm^2$, while the area net of voids, A_n, is $228900\, mm^2$:

$$A_g = 374400\, mm^2, \tag{1}$$

$$A_n = 228900\, mm^2, \tag{2}$$

$$\frac{A_n}{A_g} = 0.611. \tag{3}$$

The filling ratio of about 61% in Eq. (3) is consistent with the most widely accepted standards for semi-solid fired bricks and blocks for load-bearing walls [73] (there are still no standards on the filling ratio for semi-solid earthen load-bearing elements). According to ASTM C 652-21 [74], for example, a hollow fired brick has a minimum filling ratio of

40% and a maximum filling ratio of 75% (coring or void area greater than 25%, with a maximum of 60%). Characteristics such as redundancy, directionality and the full/empty ratio are actually crucial to guarantee the load-bearing capacity of the 3D printed walls. As these parameters change, the performance of 3D printed mono-material masonry varies, which allows the professional to design the walls for 3D printing in such a way as to achieve a wide range of functionality. Very interesting for the continuation of this line of research is therefore the performative characterization of the 3D printed walls as these parameters vary.

The printing session (March 2020) took place with the Delta WASP 3MT Industrial 4.0 LDM printer model (Figure 2), created by WASP to support research centers and laboratories in the experimentation and prototyping of components on an architectural scale. The 3D printer makes use of the Liquid Deposition Modeling (LDM) technology, which is the technology that WASP uses for its extruder for ceramic materials. Developed to achieve a level of kinematic precision very close to that of plastic polymer extruders, the LDM technology combines a screw extruder and a pressure sensor that precisely controls the flow of material and uses retraction to stop deposition. The extrusion takes place thanks to a helical screw that dispenses the right amount of material, following the instructions deriving from the G-code, moment by moment.

Figure 2. The Delta WASP 3MT Industrial 4.0 LDM (https://www.3dwasp.com/en/concrete-3d-printer-delta-wasp-3mt-concrete).

The Delta WASP 3D printer uses the “continuous feeding system” (Figure 2) which makes the pumping and feeding of the extruder continuous in a responsive way, thanks to a real-time reading system of the operating pressure at the inlet of the hose at the extruder. To obtain a good homogeneity and workability, the feeding of the 3D printer came directly from the muller that kneaded the mixture. As regards the specimen object of this paper, the extrusion setup was set with a nozzle D 30 mm (Figure 3).

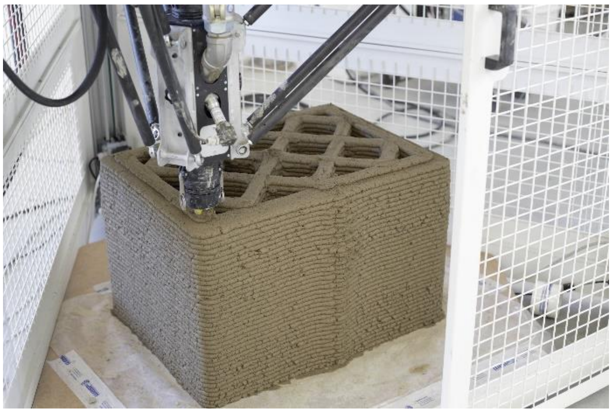

Figure 3. The 3D printing of the specimen object of this paper.

To allow comparison between the strength of the 3D printed wall segment and the average strength of the first set of cubes of [58] (Section 3.4), 3D printing of the wall segment and casting of the cubes took place on the same day and all the specimens underwent uniaxial compression test after the same curing period (90 days).

2.2 *Feasibility Assessments*

The carbonation of the aerial lime in the RH-lime bio-composite determines a production of calcium carbonate that continues indefinitely over time. This deposition mechanism is somewhat similar to the delayed precipitation of calcium carbonate that occurs due to the metabolic action of bacteria (in the MICP). These are therefore very similar stabilization mechanisms but, at the same time, of different implementation impact. In fact, while the MICP treatment consists in stimulating the growth of indigenous bacteria in situ (bio-stimulation) or increasing the ureolytic bacterial culture (bio-augmentation) [75,76], the RH-lime bio-composite is nothing more than a simple mixture of rice husk and aerial lime. Furthermore, carbonation strongly depends on the long-term stability of bacterial urease in the MICP [75,77], while it occurs spontaneously and without the need for special precautions in the RH-lime bio-composite.

The RH-lime bio-composite is also advantageous from an economic point of view. In fact, it combines lime (not particularly expensive) with RH, which is even a waste (for precision, a waste from rice processing). It is worth noting that there is a large availability of RH in the world, as rice cultivation produces a large volume of RH each year (20% to 25% by weight of the rice crop). Since this volume is used only to a small extent, as a source of renewable energy, the RH poses environmental problems related to its disposal. The two most used disposal methods, in fact, are both harmful to the environment: the first method consists in landfilling for organic waste, with potential pollution of the soil and aquifers; the second method consists in open combustion, with release of carbon dioxide in the atmosphere and potential contribution to global warming. The use in the RH-lime bio-composite for construction purposes is therefore also a viable way to reduce the environmental impact of the RH. Based on WASP's experimented data, one hectare of cultivated paddy field is able to produce 100 square meters of built area.

The construction of WASP's two full-scale housing prototypes – Gaia (Figure S1) and Tecla (Figure S2) – is a proof of the feasibility of the entire process, from architectural design and soil supply to 3D printing of entire housing modules (Figure 4). It is worth noting that Figure 4 shows two different mixing phases in the muller, the first aimed at stabilizing the soil and the second aimed at kneading the mixture. In reality, up to now WSAP has made use of only one mixing phase, which consists in simultaneously inserting all the components of the mix-design into the muller, together with the mixing water. The opportunity to carry out the mixing in two different moments is one of the results that emerged from [58], as this seems to favor the bio-cementing action of the bio-composite.

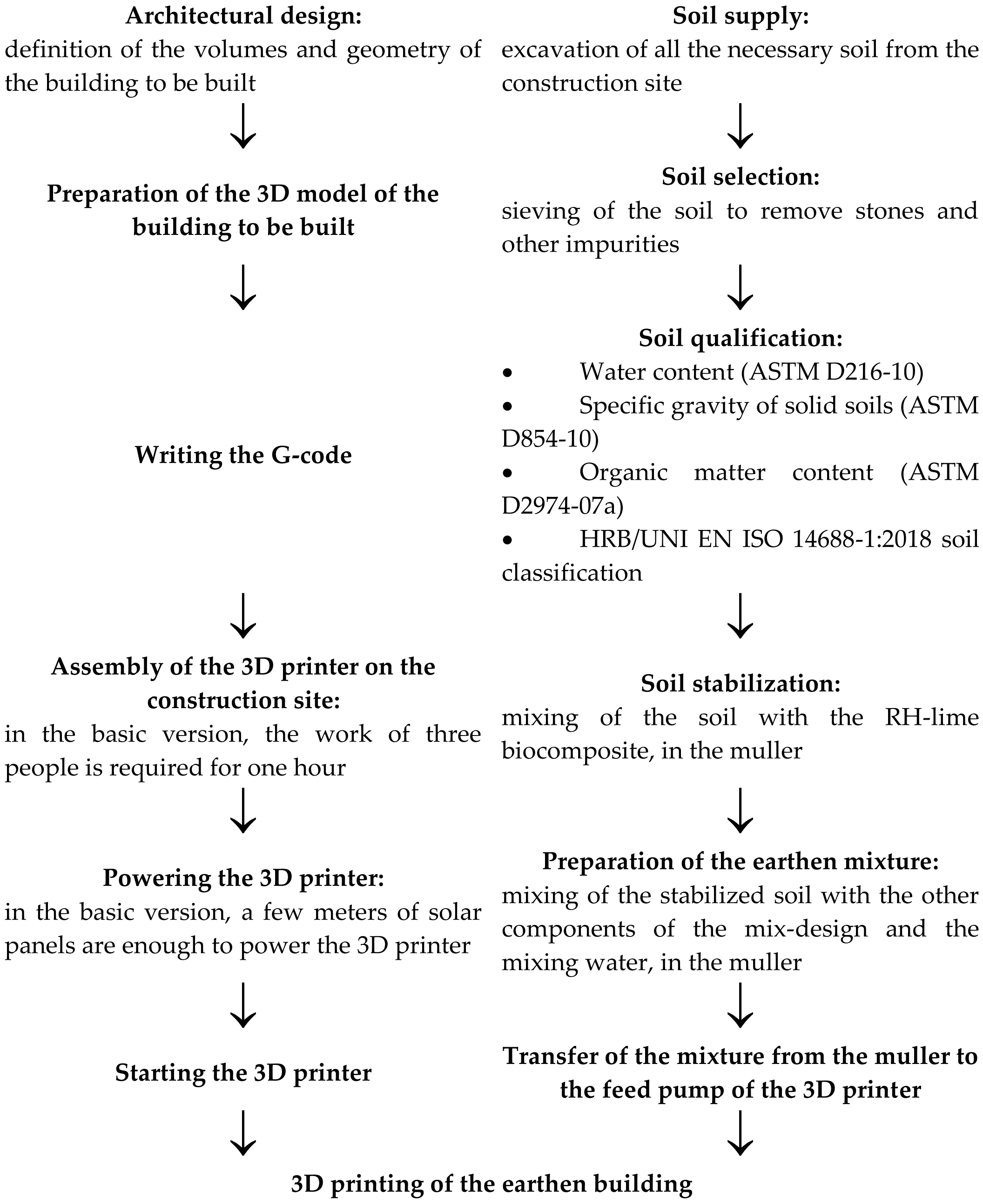

Architectural design:
definition of the volumes and geometry of the building to be built

Preparation of the 3D model of the building to be built

Writing the G-code

Assembly of the 3D printer on the construction site:
in the basic version, the work of three people is required for one hour

Powering the 3D printer:
in the basic version, a few meters of solar panels are enough to power the 3D printer

Starting the 3D printer

Soil supply:
excavation of all the necessary soil from the construction site

Soil selection:
sieving of the soil to remove stones and other impurities

Soil qualification:

- Water content (ASTM D216-10)
- Specific gravity of solid soils (ASTM D854-10)
- Organic matter content (ASTM D2974-07a)
- HRB/UNI EN ISO 14688-1:2018 soil classification

Soil stabilization:
mixing of the soil with the RH-lime biocomposite, in the muller

Preparation of the earthen mixture:
mixing of the stabilized soil with the other components of the mix-design and the mixing water, in the muller

Transfer of the mixture from the muller to the feed pump of the 3D printer

3D printing of the earthen building

Figure 4. Flowchart of the 3D printing process for earthen construction.

In its simplest version (Gaia) the WASP housing module requires only 100 hours of printing, which allows you to quickly resolve housing emergencies that may arise as a result, for example, of natural disasters.

In the WASP spirit of promoting zero-kilometer home construction, the soil used for 3D printing comes entirely from the construction site (Figure 4), which keeps construction costs very low. In fact, in addition to not requiring costs for the supply of the soil (main component of the earthen mixture, as shown in Table 1), 3D printing with soil taken from the construction site eliminates the costs of disposal of the excavated soil, which constitutes a large part of the expenses in a traditional construction. Furthermore, compared to traditional earthen constructions, 3D printing produces thicker walls using less soil, thanks to the honeycomb structure of the infill. This allows us to provide the walls with high moments of inertia to withstand horizontal loads, with a lower labor cost than massive traditional earthen structures.

Preprints (www.preprints.org) | NOT PEER-REVIEWED | Posted: 4 January 2022 doi:10.20944/preprints202112.0357.v2

Obviously, since Gaia and Tecla are prototypes, it is not yet possible to draw definitive conclusions on construction costs in a large-scale production perspective. In fact, the cost of the 3D printing activity consists of various items, the incidence of which varies, from time to time, based on the production setup: i) modeling/consulting, ii) starting the 3D printer, iii) material, iv) labor and fixed costs.

2.3 *Geometric Characteristics of the Specimen in the Fresh and Hardened States*

The fresh specimen showed ripples on the side surfaces, with a periodic pattern equal to the distance between the vertical ribs (Figure 5). Furthermore, the crossing between successive layers generated an overabundance of material that accentuated the central rib of one of the two long side faces. The enlarged rib is visible, in part, in Figure 5 (on the rear edge of the upper face) and, more in detail, in Figure 6(a,b). The excess material has also generated a deformation of the upper face, in correspondence with the enlarged rib (this deformation is visible in Figure 6(a), which a photo taken in the hardened state).

Figure 5. 3D printed specimen in the fresh state.

(**a**) (**b**)

Figure 6. 3D printed specimen in the hardened state: (**a**) excess material on the upper face; (**b**) excess material on the rear side (long side face opposite the operator).

The shrinkage suffered by the specimen during the hardening phase did not accentuate the undulation of the lateral and upper surfaces, as the shrinkage caused the same percentage variation of the lengths along all directions. Therefore, the shrinkage caused a homothetic variation in the shape of the specimen.

The extent of shrinkage is highly dependent on the mix-design, which can vary within quite wide limits in earthen mixtures, for both traditional and additive manufacturing. Thus, the percentage change in lengths caused by shrinkage is highly variable in earthen mixtures for 3D printing. This made it impossible until now to define a standard for shrinkage in extrusion earthen mixtures.

The average value reached by the linear dimensions of the wall segment in the hardened state is approximately 97.24% of the corresponding value in the fresh state, with an average (negative) percentage variation of 2.76%. Due to the dependence of shrinkage on the mix design, this value is only comparable with the data of specimens made with the same mixture, that is, the LT mix. It is therefore comparable with the (negative) percentage variation of 2.44% undergone by the cubic specimens of [58], made with the same mixture, on the same day and in the same thermo-hygrometric conditions of the wall segment. Since the casting of the cubic specimens of [58] took place by hand compaction in the formworks, the good agreement between the two shrinkage values implies that the extrusion process does not significantly alter the shrinkage behavior of the earthen mixtures. Table 2 gives the main dimensions of the specimen in the hardened state.

Table 2. Main linear dimensions of the specimen in the hardened state, after shrinkage.

Linear dimension	Value reached in the hardened state
Length	710.0 mm
Depth measured along the axis of symmetry	533.0 mm
Minimum depth between opposite ripples	515.0 mm
Height	490.0 mm
Thickness of the linear sections of the infill	35.5 mm
Thickness of the external cladding	66.0 mm

The percentage variation of the areas is equal to the square of the percentage variation of the linear dimensions. The estimated value of the nominal area after hardening is therefore equal to:

$$A_{extr} = 0.9724^2 A_n = 216439.09\ mm^2, \tag{4}$$

where A_n is the nominal area in the fresh state, given by Eq. (2).

To ensure a uniform distribution of the load on the upper face, it was necessary to remove the excess material on the upper face (Figure 7(a)) by hand sanding. This allowed the upper metal plate for load transfer (whose dimensions are in Figure 1) to adhere perfectly to the upper face of the specimen (Figure 7(b)). To allow housing the instruments on the long side faces, it was also necessary to remove the excess material of the enlarged rib (Figure 7(b)), again by sanding.

(**a**) (**b**)

Figure 7. The specimen after hand sanding: (**a**) On the upper face; (**b**) On the long side face facing the operator.

2.4 *Instrumentation for the Acquisition of the Displacements*

The acquisition of the displacements took place by means of Linear Variable Differential Transformers (LVDTs), for a total of 15 instruments. To be precise, 7 are the LVDTs

doi:10.20944/preprints202112.0357.v2

used for the acquisition of the horizontal displacements and 8 those used for the vertical displacements. Furthermore, among the 7 LVDTs for the acquisition of the horizontal displacements, 5 acquired the displacements between 2 successive vertical ribs and the remaining 2 acquired the displacements along the entire length of the long side faces. Finally, 4 of the 8 LVDTs for the acquisition of the vertical displacements measured the displacements along the 4 vertical edges of the specimen and the remaining 4 measured the displacements between opposite corners of the 2 metal plates, placed one below and one above the specimen.

Table 3 provides the labeling of the 15 LVDTs and summarizes their positioning (according to the numbering of edges and corners given in Figure 1). Figure 8 shows the 15 LVDTs after their placement.

Table 3. Labelling and positioning of the 15 LVDTs: opposite corners of the upper and lower plates have the same numbering.

Label	Direction of acquisition	Positioning
LVDT V1	Vertical	Near vertical edge 1, on the short side face to the left of the operator
LVDT V2	Vertical	Near vertical edge 2, on the short side face to the left of the operator
LVDT V3	Vertical	Near vertical edge 3, on the short side face to the right of the operator
LVDT V4	Vertical	Near vertical edge 4, on the short side face to the right of the operator
LVDT VA	Vertical	Between corner 1 of the upper plate and corner 1 of the lower plate
LVDT VB	Vertical	Between corner 2 of the upper plate and corner 2 of the lower plate
LVDT VC	Vertical	Between corner 3 of the upper plate and corner 3 of the lower plate
LVDT VD	Vertical	Between corner 4 of the upper plate and corner 4 of the lower plate
LVDT H5	Horizontal	Between the 2 ribs of the short side face to the left of the operator
LVDT H6	Horizontal	Between 2 of the ribs of the long side face in front of the operator
LVDT H7	Horizontal	Between the 2 ribs of the short side face to the right of the operator
LVDT H8	Horizontal	Between 2 of the ribs of the long side face on the opposite side of the operator
LVDT H9	Horizontal	Along the entire length of the long side face in front of the operator
LVDT H10	Horizontal	Along the entire length of the long side face on the opposite side of the operator
LVDT H11	Horizontal	Between 2 of the ribs of the long side face on the opposite side of the operator

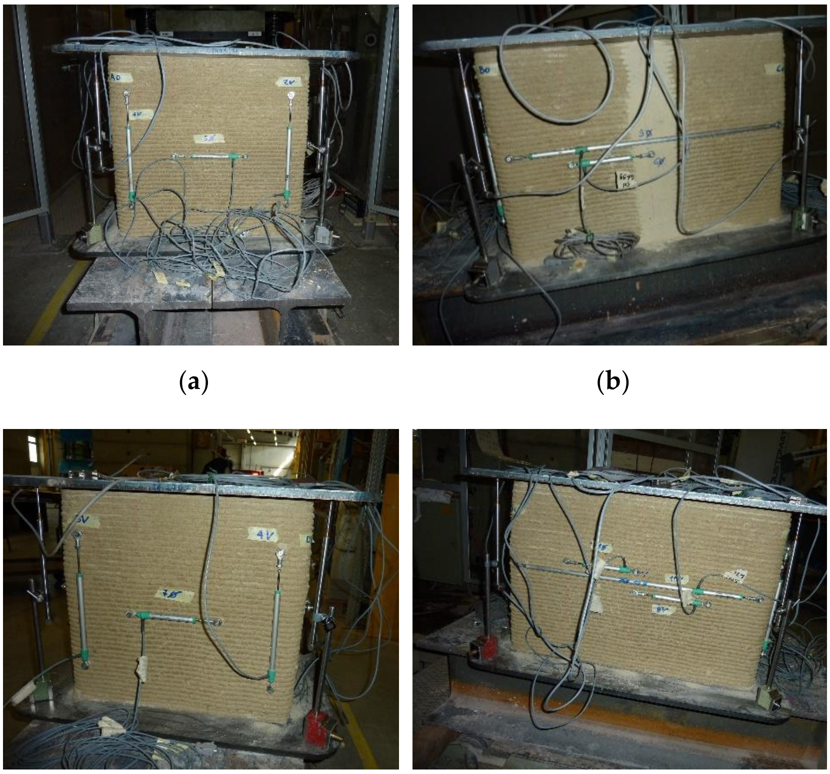

(**a**) (**b**)

(**c**) (**d**)

Figure 8. Side views of the LVDTs, listed from left to right: (**a**) LVDT VA, LVDT V1, LVDT H5, LVDT V2, LVDT VB on the short side face to the left of the operator; (**b**) LVDT VB, LVDT H9, LVDT H6, LVDT VC on the long side face in front of the operator; (**c**) LVDT VC, LVDT V3, LVDT H7, LVDT V4, LVDT VD on the short side face to the right of the operator; (**d**) LVDT VD, LVDT H10, LVDT H11, LVDT H8, LVDT VA on the long side face on the opposite side of the operator.

3 Experimental Results

The experimental results confirm what already concluded from the uniaxial compression tests on the cubic specimens made with the same mixture [58]. That is, although the load/displacement curve is similar to that typical for a brittle material, the overall behavior of the specimen presents peculiarities attributable to the rheology of the soils.

3.1 *Behavior of the Vertical Strains*

The LVDTs positioned vertically, close to the vertical edges of the specimen, returned the load/displacement curves in Figure 9, where the displacements are actually relative displacements. Specifically, a positive displacement value in Figure 9 indicates that one end of the LVDT is approaching the opposite end, which causes the instrument to shorten.

The curves in Figure 9 diverge starting from the maximum load value, which means that the upper face of the specimen underwent a significant rotation starting from the peak load. In particular, the marked snap-back – Class II behavior of rock failure under uniaxial compression, with a reduction in displacement in the post-peak region [78] – of the curve acquired through LVDT V2 is indicative of an elongation of edge 2. This means that the upward displacement caused at the top of edge 2 by the rotation of the upper face (around the testing machine head) was prevalent over the downward displacement of the testing machine head. Edge 1 also underwent some elongation after the peak, albeit to a lesser extent, causing the curve acquired through LVDT V1 to snap-back. In the opposite position to the edges 1 and 2, the rotation of the upper face has instead compressed the edges 3 and 4, resulting in a further shortening of the edges 3 and 4 with respect to that caused by the downward displacement of the head of the testing machine. This resulted in a Class I behavior of the curves acquired through LVDT V3 and LVDT V4, which means that these curves exhibited a monotonic increase in displacement after the peak. The reason for the rotation of the upper face is the failure of the short side face to the right of the operator.

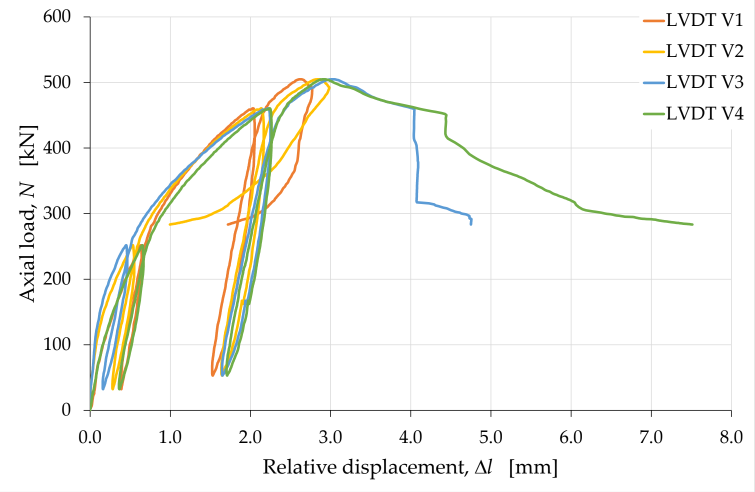

Figure 9. Load/displacement curves acquired along the vertical edges of the specimen.

Figure 10(b) shows the upper part of this side face, which undergone a detachment with sliding along an inclined plane, towards the outside. On the opposite side face, the extension due to the strong rotation of the upper face caused detachments between the horizontal layers (Figure 10(a), Figure 11).

(**a**) (**b**)

Figure 10. Failure mechanisms on the two short sides: (**a**) Side located to the left of the operator, extending between edge 1 (left) and edge 2 (right); (**b**) Side located to the right of the operator, extending between edge 3 (left) and edge 4 (right).

(**a**) (**b**)

Figure 11. Details of the detachments between the horizontal layers of the side to the left of the operator: (**a**) Left detachment, which reaches edge 1; (b) Right detachment, which reaches edge 2.

In particular, the opening of the right detachment (Figure 11(b)) is larger than the opening of the left detachment (Figure 11(a)) due to greater elongation of edge 2 compared to edge 1. After the end of the load test and removal of the specimen from the testing machine, the upper face retained a permanent value of rotation, with a left-to-right skew (Figure 12).

Figure 12. Front view of the specimen after the load test, with the upper face permanently inclined from left to right.

Due to the dependence on the rotation of the upper face, no curves among those acquired using the LVDTs V1, V2, V3 and V4 provide the axial displacement of the specimen. Consequently, none of them is useful for providing information on the rheology of the material undergoing uniaxial compression. Their average curve, on the other hand, provides the relationship between load and displacement for the points lying on the axis of the testing machine head. Since these points only move down due to the displacement of the testing machine head, the average curve expresses a relationship net of the effects of rotation. The average load/displacement curve is therefore suitable for identifying the stress/strain relationship representative of the actual uniaxial compression behavior.

Similar considerations apply to the displacements acquired at the corners of the plates (the positive values of displacement in Figure 13 indicate both the absolute downward displacements of the corners of the upper plate and the relative displacements of mutual approach between opposite corners of the upper and lower plates).

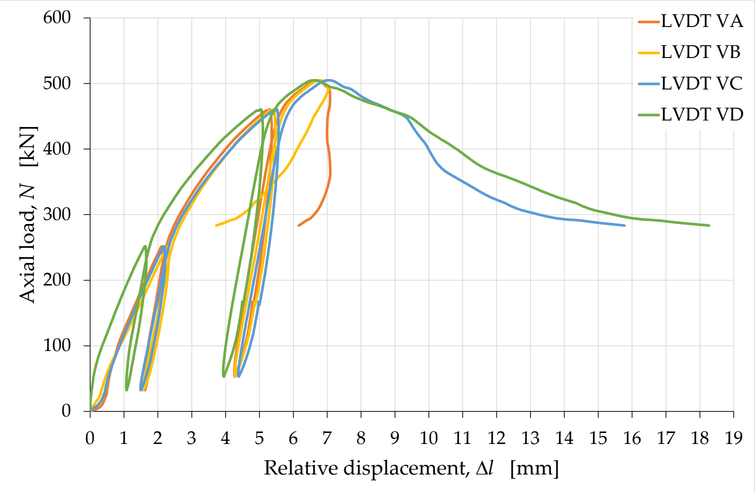

Figure 13. Load/displacement curves acquired between the corners of the metal plates for load distribution.

In fact, the vertical LVDTs VA, VB, VC and VD also provide displacement values influenced by the rotation – of the upper plate, which lies on the upper face of the specimen – because they are located far from the axis of the specimen. In particular, the curve acquired via LVDT VB (near edge 2) assumes a Class II behavior (Figure 13) as a consequence of the upward displacement of corner 2 (of the upper plate) caused by the rotation. At corner 1, the post-peak branch is, for the most part, almost vertical (curve acquired through LVDT VA in Figure 13). This means that the upward displacement caused by the rotation of the upper plate and the downward displacement caused by the movement of the testing machine head are almost perfectly balanced at corner 1. Therefore, corner 1 is close to the absolute rotation point of the upper plate. Finally, at corners 3 (near edge 3) and 4 (near edge 4) the rotation of the upper plate amplifies the downwards displacements, which gives the curves acquired via LVDT VC and LVDT VD a Class I behavior (Figure 13).

In conclusion, not even the curves with the displacements acquired at the corners of the upper plate are individually suitable for identifying the stress/strain relationship under uniaxial compression load, while their average curve is. We therefore used the average values of the (relative) displacements acquired along the edges of the specimen and at the corners of the plates – $\overline{\Delta l}_e$ and $\overline{\Delta l}_c$, respectively – to identify the vertical strains along the axis of the specimen:

$$\overline{\Delta l}_e = \frac{1}{4}(\Delta l_{V1} + \Delta l_{V2} + \Delta l_{V3} + \Delta l_{V4}), \tag{5}$$

$$\overline{\Delta l}_c = \frac{1}{4}(\Delta l_{VA} + \Delta l_{VB} + \Delta l_{VC} + \Delta l_{VD}), \tag{6}$$

where Δl_{V1}, Δl_{V2}, Δl_{V3}, Δl_{V4}, Δl_{VA}, Δl_{VB}, Δl_{VC} and Δl_{VD} are the relative displacements (shortenings) acquired, respectively, by the LVDTs V1, V2, V3, V4, VA, VB, VC and VD.

The vertical strain ε_e is then the ratio of $\overline{\Delta l}_e$ to the length of the LVDTs placed along the edges of the specimen, l_{V_e}, and ε_c is the ratio of $\overline{\Delta l}_c$ to the length of the LVDTs placed between the corners of the upper and lower plates, l_{V_c}:

$$\varepsilon_e = \frac{\overline{\Delta l}_e}{l_{V_e}}, \tag{7}$$

$$\varepsilon_c = \frac{\overline{\Delta l}_c}{l_{V_c}}. \tag{8}$$

Figure 14 shows the stress/strain curves obtained for ε_e and ε_c (positive strain values indicate shortening in the axial direction), with the axial stress, σ_v, given by the ratio between the axial load, N, and the extruded area net of shrinkage phenomena, A_{extr}:

$$\sigma_v = \frac{N}{A_{extr}}, \tag{9}$$

where A_{extr} is the nominal area in Eq. (4).

The greater deformability of the curve for ε_c compared to the curve for ε_e indicates that the deformation phenomena are more intense near the contact areas of the specimen with the external load. The localization of the strains close to the plates of the testing machine is particularly evident in the early stages of the load test, that is, near the origin of the diagrams in Figure 14. In fact, it is precisely near the origin that we can observe the greatest difference between the slopes of the two curves and, since these are stress/strain diagrams, their slopes represent stiffnesses. In the following, when we will talk about vertical strains, ε_v, we will refer to the values of strains obtained from the average displacements at the corners.

$$\varepsilon_v = \varepsilon_c. \tag{10}$$

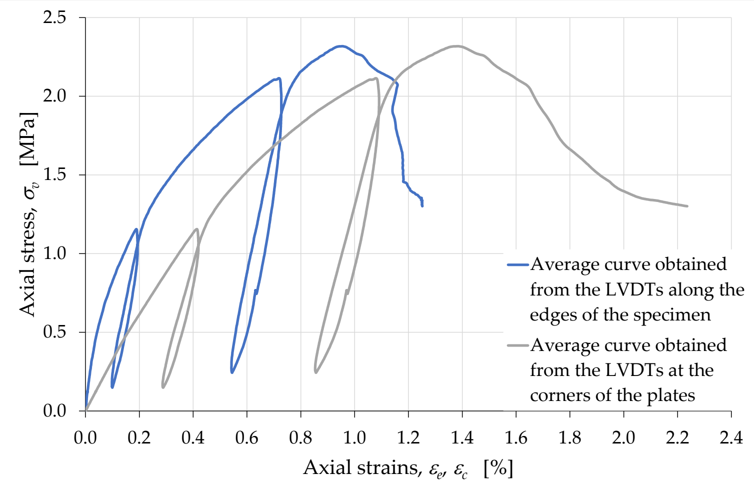

Figure 14. Average curves of the axial stress with respect to the axial strains ε_e and ε_c.

If compared with the stress/strain diagrams of [58], Figure 14 provides information on the effects induced by the extrusion process on the mechanical properties of the mixture. In fact, the slopes in Figure 14 are monotonically non-increasing functions up to the peak (excluding the unloading/reloading cycles), while the branches between the origins and the peaks in [58] have 2 points of inflection each, due to the closing of the voids during the compression test. Since the specimens in [58] were compacted by hand in the formworks, this means that the pressure to which the mixture is subjected in the extruder is able to close the voids in the mixture to a greater extent than manual compaction does.

Figure 14 also provides indirect indications on the damage phenomena that develop inside the specimen during the compression test. In particular, this information derives from the average slopes of the unloading/reloading cycles [79], as their variation provides an empirical evaluation of the damage parameter (Figure S3). Since the average slope of unloading/reloading is almost the same for both cycles in Figure 14 (in both the ε_e curve and the ε_c curve), we can conclude that the damage effects are balanced by the opposite effects of the material compaction due to the increasing compressive load [58], at least as regards the growing branch of the stress/strain curves. It is worth noting that this balance of effects is peculiar to earthen mixtures and is not specific to the behavior of brittle construction materials. Being much less compressible than earthen mixtures, brittle construction materials have in fact unloading/reloading slopes that decrease as the load test proceeds (Figure S4). Therefore, the constancy of the unloading/reloading slopes is one of the results that characterize the earthen mixture as a material with hybrid characteristics, halfway between a soil and a properly called brittle material.

3.2 *Behavior of the Horizontal Strains*

The relationship between horizontal and vertical strains turned out to be that typical of solid mechanics, characterized by elongations (negative strains in Figures 15–19) along the directions orthogonal to that of the mono-axial compressive load (Poisson effect).

The LVDTs placed horizontally allow us to draw more than one conclusion about the horizontal strains, which turned out to be very small in all cases (in Figures 15–19, we excluded the data acquired by LVDT H8, due to instrumental errors). The first observation we want to focus on concerns the comparison between the horizontal strains estimated over the inter-rib length of the ribs described in Section 2.3 (Figure 15) and the horizontal strains estimated over the entire length of the side faces (Figure 16). This comparison does not reveal evident localization phenomena of the horizontal strains, since the average curve obtained over the inter-rib length differs by minimal quantities from the average curve obtained over the entire length of the side faces (Figure 17).

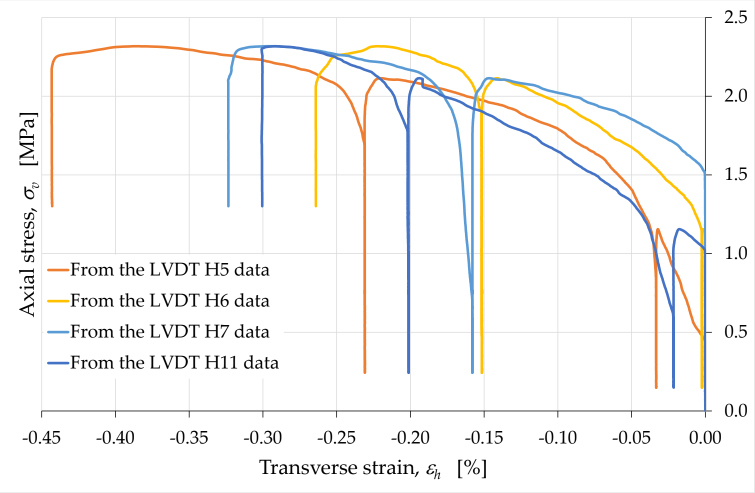

Figure 15. Axial stress/transverse strain curves acquired by the horizontal LVDTs between the ribs.

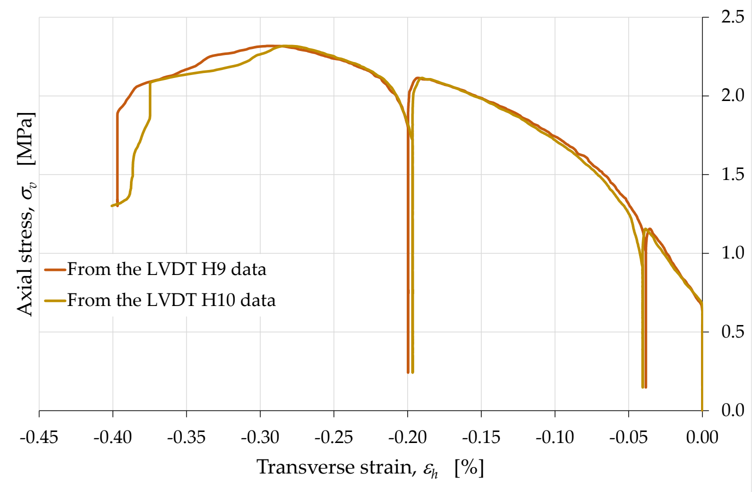

Figure 16. Axial stress/transverse strain curves acquired over the entire length of the long side faces.

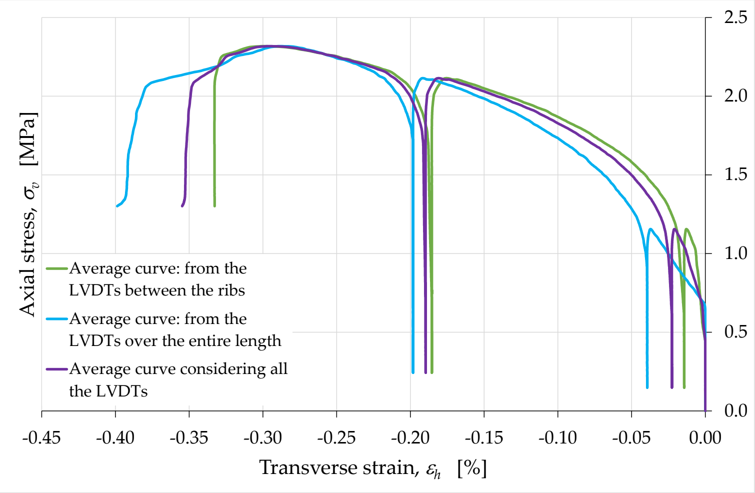

Figure 17. Average curves of axial stress with respect to transverse strain, obtained from the relative displacements over the inter-rib length and over the entire length of the long side faces.

Therefore, the presence of an infill does not have a significant effect on the strains of the external envelope. In other words, despite the presence of hollow areas inside the specimen, the overall behavior is that typical of a solid without cavities. In particular, the almost complete superimposition of the two curves of Figure 16 shows that the two long side faces (one in front of the operator and one on the opposite side) have undergone the same deformation history.

The average curves obtained for the long sides (from the values of the LVDTs H6, H9, H10 and H11) and for the short sides (from the values of the LVDTs H5 and H7) confirm the conclusions about the role of the internal infill (Figure 18). In fact, even in the latter case the difference between the two average curves is minimal.

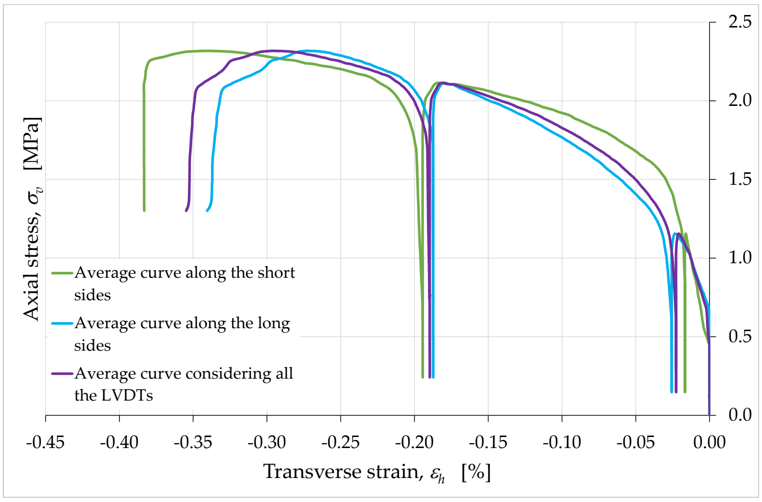

Figure 18. Average curves of axial stress with respect to transverse strain, obtained from the relative displacements over the short and the long side faces.

We can therefore assume that the average strain along the horizontal direction of the long side faces, ε_{h_1}, is equal to the average strain along the horizontal direction of the short side faces, ε_{h_2}:

$$\varepsilon_{h_1} = \frac{1}{4}\left(\frac{\Delta l_{H6}}{l_{H6}} + \frac{\Delta l_{H9}}{l_{H9}} + \frac{\Delta l_{H10}}{l_{H10}} + \frac{\Delta l_{H11}}{l_{H11}}\right) = \frac{1}{4}\left(\frac{\Delta l_{H6} + \Delta l_{H11}}{l_{H_r}} + \frac{\Delta l_{H9} + \Delta l_{H10}}{l_{H_s}}\right), \quad (11)$$

$$\varepsilon_{h_2} = \frac{1}{2}\left(\frac{\Delta l_{H5}}{l_{H5}} + \frac{\Delta l_{H7}}{l_{H7}}\right) = \frac{1}{2}\frac{\Delta l_{H5} + \Delta l_{H7}}{l_{H_r}}, \quad (12)$$

$$\varepsilon_{h_1} = \varepsilon_{h_2} = \varepsilon_h, \quad (13)$$

where:

- Δl_{H5} is the elongation of LVDT H5;
- Δl_{H6} is the elongation of LVDT H6;
- Δl_{H7} is the elongation of LVDT H7;
- Δl_{H9} is the elongation of LVDT H9;
- Δl_{H10} is the elongation of LVDT H10;
- Δl_{H11} is the elongation of LVDT H11;
- $l_{H5} = l_{H6} = l_{H7} = l_{H11} = l_{H_r}$ is the length of the LVDTs between the ribs;
- $l_{H9} = l_{H10} = l_{H_s}$ is the length of the LVDTs that extend along the entire long side faces.

The equalities in Eq. (13) mean that the specimen is transversely isotropic, that is, isotropic in the cross section.

The peculiarity of the horizontal strain curves in Figures 15–18 concerns the behavior during the unloading/reloading cycles. In fact, unlike what happens for the vertical strains, the unloading/reloading cycles in Figures 15–18 do not show a hysteretic behavior and follow a vertical path. This highlights a clear difference in behavior between the horizontal strains, ε_h, and the vertical strains, ε_v (Figure 19).

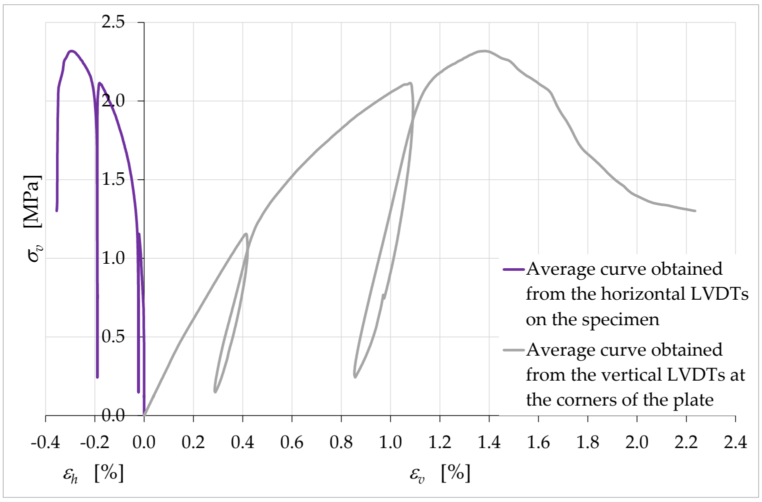

Figure 19. Average curves of axial stress with respect to axial and transverse strain.

In particular, the absence of a hysteretic behavior for ε_h indicates the non-occurrence of dissipative effects along the horizontal direction (while they occur along the vertical direction). The vertical path of the ε_h cycles, on the other hand, provides information on the elastic and plastic components of the horizontal strain. In fact, since the elastic strain is the strain recovered at the unloading, we can conclude that the strain that occurs in the horizontal direction has only a plastic component (not recoverable at the unloading). Since the horizontal direction is also the extrusion direction, it therefore appears that the extrusion process has a decisive effect on the rheology of the extruded material, imparting only the plastic component to the strains along the extrusion direction. Along the direction orthogonal to that of the extruded layers, however, the strains show both the plastic and the elastic component (Figure 19).

We can therefore speak of anisotropy induced by the extrusion process. To be precise, since the specimen is transversely isotropic due to Eq. (13), the overall behavior of the specimen is orthotropic. The main consequence of the orthotropy induced by the extrusion process is the invariance of the linear dimensions of the cross section at the removal of the axial load.

3.3 *Relationships between Strains*

Figure 19 also provides information on the ratio between the horizontal strains, ε_h, and the vertical strains, ε_v. In continuum mechanics, the negative of this ratio gives the value of Poisson's ratio, ν, which is the negative of the ratio of transverse strain to axial strain:

$$\nu = -\frac{\varepsilon_h}{\varepsilon_v}. \tag{14}$$

Strictly speaking, in mechanical testing it is incorrect to continue to give the ratio in Eq. (14) the name of Poisson's ratio, for at least two reasons. The first reason is that Poisson's ratio is one of the elastic coefficients that define Hooke's law in linear elastic regime, while the loads of the uniaxial compression test lead the material well beyond its own range of linear elastic behavior. The second reason is that the macro-cracks that propagate inside the specimen during the test (Figures S5(a,b)) does not allow treating the specimen as a continuum [80], making it impossible to use the definitions of the continuum mechanics. For the same reason, it is also necessary to revise the definitions of ε_h and ε_v, which lose the meaning of local deformations at the point they have in continuum mechanics. In analogy to the definition of engineering strains, they are the ratios of relative displacements (between points) to the reference lengths. During a mechanical tests, however, the (relative) displacements between points can occur due to both the deformation of the body (rheological behavior) and the opening of cracks (non-rheological behavior), which results

doi:10.20944/preprints202112.0357.v2

from the rigid body motions of the new surfaces generated by the cracks [81]. This deprives the ratio between engineering strains of rheological significance. Therefore, we will continue to refer to the ratio ν in Eq. (14) as the negative of the ratio of (engineering) strains along two orthogonal directions, avoiding calling it Poisson's ratio.

Due to the small values of ε_h until the end of the load test, ν maintains unusually low values for a brittle construction material. As an example, Table 4 provides the values of ν for a few instants of the uniaxial compression test on the wall segment.

Table 4. Some of the values assumed by the coefficient ν during the test.

Stress value	ν
Half the stress of first unloading	0.008
Stress at the beginning of the first unloading/reloading cycle	0.051
Stress at the beginning of the second unloading/reloading cycle	0.168
Maximum stress	0.214
Ultimate stress	0.159

The trend of the values in Table 4 is very unusual for a brittle construction material. In fact, ν is first increasing and subsequently decreasing, while in brittle construction materials it is increasing for the entire duration of the uniaxial compression test (Figure S6: curve with the transverse strain acquired on the external surface, by means of the strain gauge of Figure S7(a)). Furthermore, it is worth remembering that values close to zero of ν are characteristic of open-cell polymer foams due to the tendency of the cells to collapse under compression [82]. Therefore, such low values of ν in Table 4 suggest that the extruded earthen materials have a high number of voids that tend to collapse during the compression test. According to the curve of the horizontal strains in Figure 19 and to the values of ν in Table 4, in the case of earthen materials the voids tend to collapse mainly at the beginning of the compression test and after the peak of the stress/strain curve. As for the reason for the presence of such a large number of voids, it may depend both on the high percentage of soil in the mixture and on the layer-by-layer extrusion process.

From Figure 20, which is the graph of the values of ν versus the axial strain, ε_v, it results that the increase in ν ends at $\varepsilon_v = \hat{\varepsilon}_v$, which is the strain at the maximum stress of the stress/strain curve, $\sigma_{v_{max}}$ (Figure 19):

$$\hat{\varepsilon}_v = \varepsilon_v|_{\sigma_v=\sigma_{v_{max}}} \cong 1.4\%. \tag{15}$$

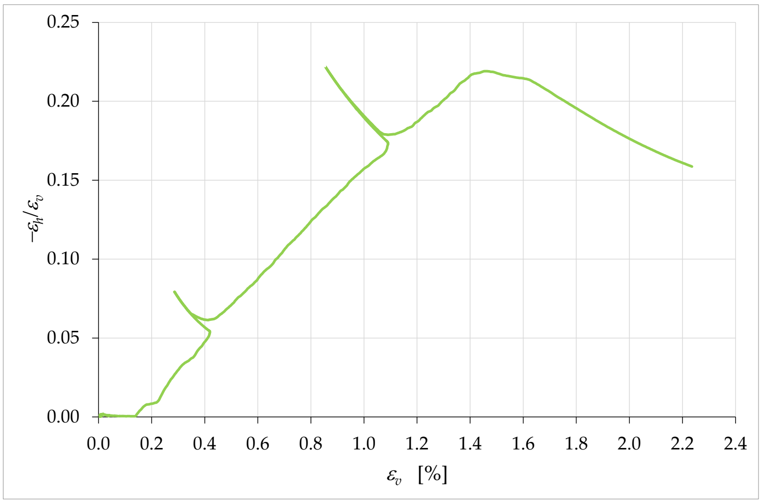

Figure 20. Curve of ν (apparent Poisson's ratio) with respect to the axial strain, ε_v.

Then, ν assumes an almost constant behavior at first and, subsequently, decidedly decreasing. It is worth noting that the last point of the curve in Figure 20 is not indicative of the actual failure of the specimen. In fact, since the LVDTs showed a tendency to detach from the specimen in the final stages of the test, it was preferred to interrupt the acquisition of the displacements and remove the LVDTs in advance, to protect the instruments from damage due to a fall. Therefore, the curve actually continues beyond the last acquisition point. The slope of the curve at the last point suggests that the final value of ν could be significantly lower than the last identified value, equal to 0.159 (Table 4).

Figure 20 also shows near zero values of ν for the linear elastic regime, which indicates the tendency of the specimen to collapse on itself without lateral expansion. Both the decreasing behavior after the maximum load and the values close to zero in the linear elastic regime are absolute novelties for the ratio ν of a brittle construction material. As with the collapse of voids, these behaviors could actually derive from the properties of the soil that makes up a large part of the mixture.

Equally surprising for a brittle construction material is the sum of the strains along the three orthogonal directions of the axis and the two horizontal sides (Figure 21):

$$\varepsilon_\theta = \varepsilon_v + \varepsilon_{h_1} + \varepsilon_{h_2} = \varepsilon_v + 2\varepsilon_h, \tag{16}$$

where we made use of Eq. (13).

In continuum mechanics, ε_θ is the volumetric strain, that is, the ratio of the change in volume of a body, ΔV, to the original volume of the body, V:

$$\varepsilon_\theta = \frac{\Delta V}{V}. \tag{17}$$

Due to crack propagation, however, the rigid body motions of the crack surfaces also affect the sums in Eq. (16) [83]. Consequently, like ν, also ε_θ has no real rheological significance in a mechanical test, but is indicative of an average behavior at the mesoscale.

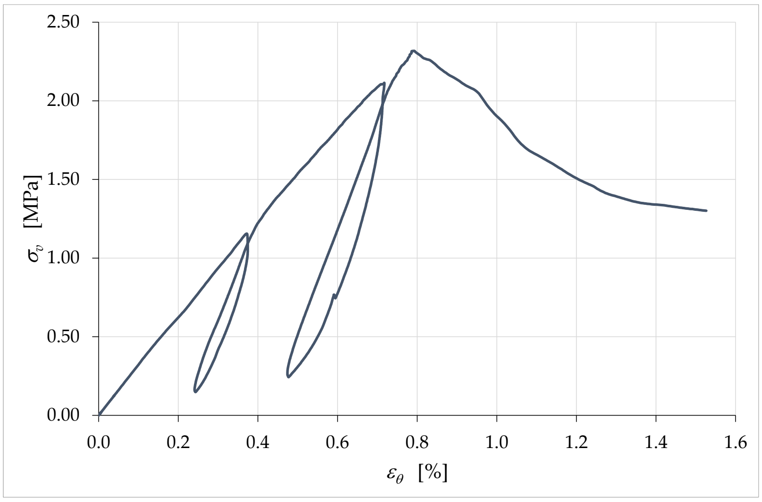

Figure 21. Curve of the axial stress, σ_v, with respect to ε_ϑ (apparent volumetric strain).

Between the origin and the peak (where $\sigma_v = \sigma_{v_{max}}$), the values of ε_θ in Figure 21 are very close to being directly proportional to the axial stress, σ_v (positive values of ε_θ in Figure 21 imply a decrease in volume). This does not correspond to the behavior of ε_θ for brittle construction materials, such as concrete (Figure S8: curve with the transverse strain acquired on the external surface, by means of the strain gauge in Figure S7(a)). Indeed, the ε_θ curve between the origin and the peak of brittle construction materials changes from being concave (concave downward) to convex (concave upward).

The nearly linear behavior up to the peak in Figure 21 makes K, the ratio between σ_v and ε_θ, almost constant up to the peak:

$$K = \frac{\sigma_v}{\varepsilon_\theta}. \tag{18}$$

In Figure 22, this means that K is almost constant in the range $0 \leq \varepsilon_v \leq \hat{\varepsilon}_v$, with $\hat{\varepsilon}_v$ defined in Eq. (15).

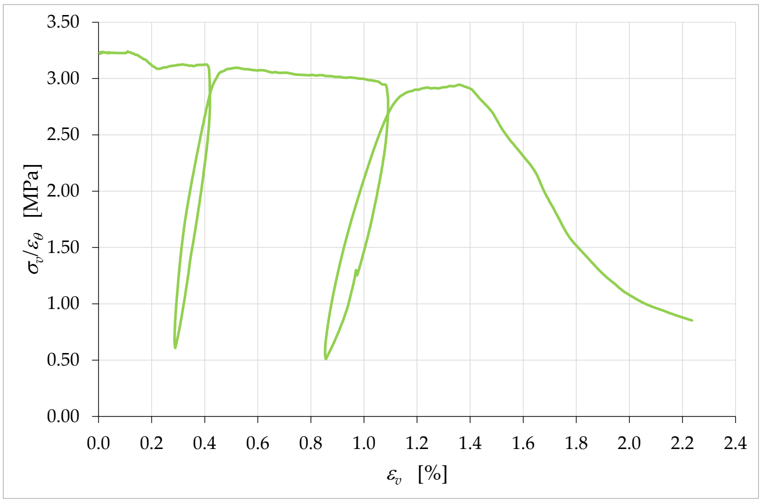

Figure 22. Dependence of the ratio K on the axial strain, ε_v.

Continuing the comparison between the behavior of brittle materials and earthen mixtures, the convex branch of the ε_θ curve of brittle materials assumes a vertical tangent for a stress value less than the maximum stress (Figure S8: curve with the transverse strain acquired on the external surface). Subsequently, the values of ε_θ begin to decrease so much to change sign and the curve becomes concave again (Figure S8: curve with the transverse strain acquired on the external surface). The change in sign of ε_θ indicates an increase in the volume of brittle specimens, which reach a final volume greater than the original volume (dilative behavior) [83–85]. In Figure 21, on the contrary, the curve ε_θ never assumes a vertical tangent and ε_θ is an ever-increasing function. This means that the earthen specimens have a contractive behavior until the end of the test, while the brittle materials become dilative after the maximum load.

Obviously, all of the above is valid within the limits of the two components, one rheological and one not, which make up the (relative) displacements acquired on the external surface of the specimen. It is worth noting, in fact, that, if we identify the strains net of the non-rheological components [83], ε_θ is an ever-increasing function (in absolute value) even in brittle construction materials (Figure S8: curve with the transverse strain acquired inside the resistant structure, by means of the fiber optic sensor in Figure S7(b)). Even the values of ν changes in the latter case, causing the ν/ε_v curve of brittle construction materials to decrease (in absolute value) in the final branch (Figure S6: curve with the transverse strain acquired inside the resistant structure, by means of the fiber optic sensor in Figure S7(b)). We can therefore interpret the ever-increasing behavior of ε_θ in Figure 21 and the negative slope of the last branch of the ν/ε_v curve in Figure 20 as indications that, in earthen materials, the non-rheological component of the displacement is negligible compared to the rheological component. This means that earthen materials under uniaxial compression load tend to develop far fewer cracks than brittle construction materials do, which confirms the conclusions we had reached based on the slope of the unloading/reloading cycles in Figure 14. In conclusion, the analysis of the strains developed during a uniaxial compression test confirms that the extrusion process of earthen mixtures results in a material with peculiar mechanical properties – at the mesoscale – halfway between those of a brittle material and a soil.

3.4 Failure Mechanisms and Compressive Strength

The failure of the specimen began at the contact edges between the specimen and the plates, with the enucleation of inclined sliding planes that propagated towards the interior of the specimen. This led to the specimen cracking along the vertical edges and the outward ejection of the outermost part of the specimen (Figure 23). However, there was no real collapse of the external part, not even at the end of the load test (Figure 23).

Figure 23. Appearance of the specimen after raising the head of the testing machine.

The manual removal of the external cladding material (Figure 24(a)) – isolated only in part by the sliding surfaces – has highlighted the double truncated pyramidal structure of the internal part (Figure 24(b)), which retained a fair capacity to withstand loads. This failure mechanism is similar to that observed in cubic and cylindrical concrete specimens, when subjected to uniaxial compression tests (Figure S5). It is worth noting, however, that, unlike what happens in concrete, the damaging mechanism of the earthen specimen affected only the outermost part, stopping at the internal infill. In fact, it seems that the honeycomb structure of the infill is able to interrupt the propagation of the macro-cracks towards the inside, preserving the infill itself from the main damage mechanisms (Figure 25(a)). Only minor crushing damage, mainly located near the external contour, affected the internal filling (Figure 25(b)).

(**a**) (**b**)

Figure 24. Side views of the specimen after the test: (**a**) Before and (**b**) after the removal of the material isolated (only in part) by the sliding surfaces.

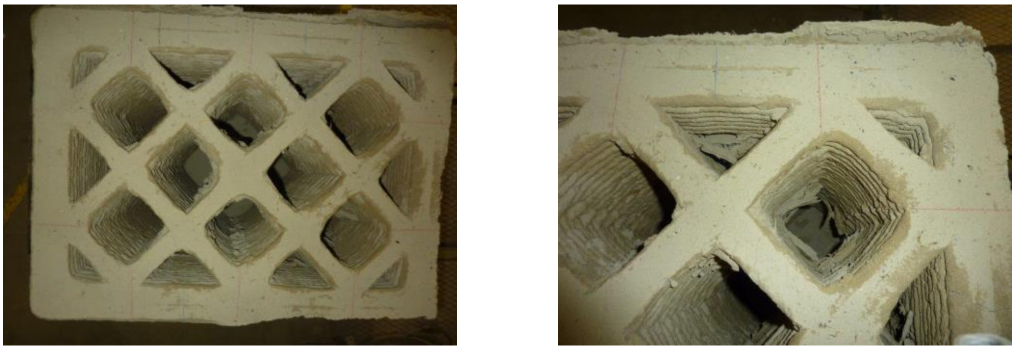

(**a**) (**b**)

Figure 25. Top view of the specimen after the test: (**a**) Overall view (**b**); Detail of the corner at the top right.

The crack stopper action exerted by the infill is also decisive in determining the shape of the stress/strain curve. The σ_v/ε_v curve in Figure 26 differs from the σ_v/ε_c curve in Figure 14 only in the range of displayed data. In fact, as previously mentioned, it was preferred to remove the LVDTs installed on the surface of the specimen in advance, to avoid damaging the instruments. For purposes of comparison, in Figure 14 this resulted in truncating the curve σ_v/ε_c at the instant of the last LVDT acquisition on the specimen surface. Since the LVDTs placed between the corners of the plates did not suffer any danger of damage, they actually continued to acquire the displacements until the end of the compression test. Figure 26 therefore shows the stress/strain curve obtained from the acquisitions at the corners up to the test end, which did not coincide with the failure of the specimen. The interruption of the test was in fact necessary in any case in advance, to avoid that the LVDTs at the corners of the plates went out of scale.

The larger set of data in Figure 26 allows us to appreciate the shape of the final part of the σ_v/ε_v curve, which tends asymptotically to a horizontal plateau. When compared with the stress/strain curves of brittle construction materials (Figure S9), even this plateau exhibits unusual behavior, although brittle construction materials may also have asymptotic final behavior. In fact, the softening branch in Figure 26 seems to find an asymptotic limit for a fraction of the maximum stress significantly greater than that typical of brittle construction materials (strain-softening is a decline of uniaxial stress at increasing strain [86]). To give an idea of the order of magnitude of the quantities involved, the ultimate stress in Figure 26 is approximately 53% of the maximum stress, while the ultimate stress of brittle construction materials is close to zero.

The responsible of this anomalous behavior is not the bio-stabilizing effect of the RH, as previous studies on cast specimens made with bio-stabilized earthen mixtures have never shown a high residual stress plateau [61,87]. Rather, the high value of ultimate stress (as a percentage of the maximum stress) can find an explanation precisely in the crack stopper action of the infill. Indeed, experimental [80] and numerical [88] studies on the shape-effect of brittle solids showed that the softening branch is steeper when the damage phenomena are more developed. Consequently, the softening branch provides indirect information on the resistant cross-section, because the area of the resistant cross-section (resistant area) – which decreases faster when the damage phenomena develop faster (Figure S3) – decreases faster even when the softening branch is steeper [89]. Therefore, an asymptotic behavior with a high value of residual stress is symptomatic of a crack pattern that only partially affected the resistant cross-section. In the specific case of a 3D printed wall segment, it is also a proof of the effectiveness of the infill in blocking the propagation of cracks. This gives a physical meaning to the final plateau of the softening branch, allowing us to state that the higher the plateau the greater the resistant area at the end of test. Thus, the shape of the curve in Figure 26 reveals that a 3D printed specimen made of earthen material retains a greater resistant area than an identical specimen made of brittle construction material does.

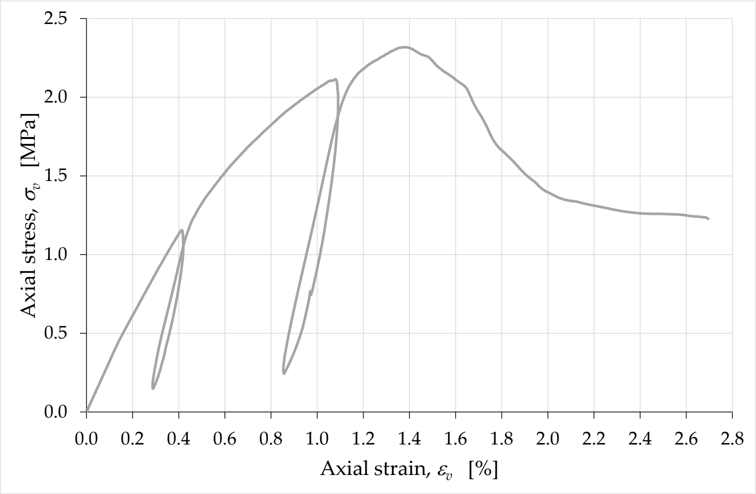

Figure 26. Complete average curve of the axial stress with respect to the axial strain, obtained from the acquisitions of the LVDTs placed between the corners of the metal plates for the distribution of the load.

As far as strength is concerned, the maximum stress in Figure 26 is equal to 2.32 MPa. This value falls within the dispersion range of the strength at 90 days of curing evaluated on cubic specimens made with the same earthen mixture and compacted by hand in the formworks [58], with an average value of 2.50 MPa. This means that, along the direction orthogonal to the layers, the layer-by-layer extrusion process did not substantially change the strength of the earthen material compared to that of the hand-compacted material. In other words, the 3D printing process was good enough to avoid decay in mechanical strength properties due to imperfect cohesion between superimposed layers.

The good cohesion between the extruded layers is also evident in Figure 27, which shows a sliding plane that intersects several layers in the outer envelope. In Figure 27, in fact, there are no evident discontinuities between the layers, nor are there any detachments between the two shells that make up the external envelope (Figure 1). On the other hand, the external part of the specimen can develop the same sliding planes of a homogenous material, cast in the formwork, precisely because of the good cohesion between its extruded layers.

Figure 27. Appearance of the extruded layers along one of the sliding surfaces activated by crack propagation.

The compressive strength value of 2.32 MPa is a good result for a 3D printed load-bearing earthen element, as it is slightly higher than the minimum compressive strength required for one-story external walls of rammed earth (2 MPa) [36].

Preprints (www.preprints.org) | NOT PEER-REVIEWED | Posted: 4 January 2022 doi:10.20944/preprints202112.0357.v2

4 Discussion

The main motivation of the experimental test presented in this paper was to investigate the major criticalities under uniaxial compression load of a 3D printed wall segment made with an earthen mixture, in view of possible uses for the construction of multi-story buildings. The results of the compression test showed that the two possible criticalities identified a priori – namely the low degree of collaboration between the layers and the overturning of the external envelope – do not actually constitute real dangers for the stability of the earthen structure under vertical loads. As far as the first criticality is concerned, in fact, the layers showed sufficient cohesion to resist the loads as a single rigid body, so much so that the sliding surfaces show the same peculiarities of compact materials and the strength is comparable to that of cubic specimens made with the same mixture. Regarding the second criticality, the load test actually showed a tendency to detachment of the lateral faces, but the very small Poisson's ratio kept the outward displacements so low as not to cause overturning problems. The specimen rather showed a tendency to implosion, especially at the beginning and end of the load test.

4.1 *Main Findings*

The experimental results made it possible to obtain more information than what we had set out to get from this experimental test, that is, the verification of the cohesion between layers and the sensitivity to overturning of the lateral faces. Some of this information is particularly important, because it characterizes the earthen mixture as a material that does not fit perfectly into the class of brittle construction materials, therefore deserving of a separate classification. In fact, if studied at the mesoscale, the earthen mixture provides values of (apparent) Poisson's ratio (ν) and (apparent) volumetric strain (ε_θ) that have little to do with the homologous quantities of brittle construction materials. The major anomalies with respect to the typical mechanical behavior of brittle construction materials consist of:

- Values close to zero of ν in linear elastic regime (implosive behavior);
- Low values of ν for the entire duration of the compression test;
- Decreasing values of ν in the final part of the compression test;
- (almost) Direct proportionality between ε_θ and the axial stress, σ_v, up to the maximum load;
- Increasing values of ε_θ (contractive behavior) until the end of the compression test;
- Stress/strain curve with asymptotic behavior towards an ultimate stress value equal to about 50% of the maximum stress.

From the comparison with the studies for the experimental identification of the damage parameter in concrete solids, it emerged that all these anomalies, apart from the first one, depend on the ability of the internal infill to stop the propagation of macro-cracks inside the specimen. This has direct repercussions on the value of the resistant area, which decreases much more slowly in the earthen solid than in a full solid of identical external dimensions, made of concrete. From the point of view of identifying the constitutive relationship, this means that the difference between mesoscale and microscale behavior is much less marked for earthen material than it is for concrete.

By reversing the point of view, the crack stopper action of the internal infill can find applications for design purposes. In other words, it is possible to give the resistant area of the 3D printed load-bearing earthen elements characteristics as similar as possible to any specific desired behavior, simply by adequately designing the internal infill. This gives the internal infill a real structural function.

As far as the first anomaly is concerned, it is likely that it depends on the presence of a high percentage of voids, which tend to collapse during the compression test. Even the results of a previous experimental campaign on the strength of cubic specimens compacted in formwork showed that the earthen mixture has a high percentage of voids. The value close to zero of ν in linear elastic regime is therefore a rheological property, which depends on the granulometric melt of the mixture. Specifically, it depends on the fractions of the mixture that have the greater grain size and on the low percentage of fine fractions.

From this experimental test a further result emerged, namely the orthotropic behavior of the earthen specimen. In particular, the behavior turned out to be isotropic in the cross-section, but different from the behavior along the axial direction. The reason for the orthotropy lies in the changes to the rheology of the mixture that follow from the extrusion process. The high pressure undergone by the mixture during extrusion, in fact, seems to plasticize the mixture along the direction of extrusion. The plasticization is such that the displacements in the cross-section are non-recoverable at all, at the unloading. Along the axial direction, however, the displacements also have an elastic component, recoverable at unloading.

4.2 *Limitations of the Study*

Usually, the uniaxial compression tests on specimens tested in the laboratory only provide a partial view of the behavior of the material in place, as they do not take into account the confinement effect exerted between contiguous elements. In other words, meaning a wall as formed by many contiguous wall segments, each segment limits the free lateral expansion of the continuous segments by imparting horizontal forces that modify the overall compressive strength (due to the Poisson effect). Since the uniaxial compression test does not provide horizontal forces to the specimen, this test is therefore not representative of the actual behavior of the material in place. A further cause of non-representativeness of the actual behavior of the uniaxial compression test is the development of inclined sliding planes, which cause a decrease in the resistant area of the specimen.

In the specific case of the 3D printed earthen wall segment, however, the behavior under uniaxial load of the specimen is reasonably representative of the load-bearing capacities of the entire wall. In fact, the value close to zero of Poisson's ratio makes the interactions between contiguous vertical elements very low and the crack stopper action of the infill allows the resistant area to differ slightly from the nominal area.

The reasons for uncertainty about the experimental result lie rather in the environmental conditions. Both the 3D printing process and the curing of the wall segment took place in the laboratory, under controlled thermo-hygrometric conditions. This is important for the replicability of the experimental results but it is also the major limitation of this study. Indeed, in the spirit of a zero-kilometer construction, WASP's 3D printing technology consists of on-site printing of buildings, with the transport of the 3D printer to the construction site. Since the thermo-hygrometric conditions of the construction site depend on the local environmental conditions, the printing process of a building can also take place in conditions that are very different from those controlled in the laboratory. This has an impact primarily on the volume of mixing water. For example, printing in very hot climates may require more mixing water to counteract the decay of fluidity due to strong evaporation. Since the compressive strength depends on the volume of mixing water, the local environmental conditions at the time of printing have an impact on the compressive strength of the building. In addition, as the local temperature and humidity vary continuously over the time span of the printing process – which takes a few days of work – the volume of mixing water requires continuous recalibration over the course of a printing day. This may result in different compressive strengths for the building portions printed under different thermo-hygrometric conditions. Therefore, in addition to the orthotropy caused by the extrusion process (Section 3.2), earthen buildings printed on-site may suffer from an anisotropic effect, of a degree not known a priori, due to the changing environmental conditions of the construction site.

To verify the actual impact of the environmental conditions on the compressive strengths, it may be appropriate to subject to uniaxial compression testing and compare the results of some mixture samples taken from the muller at different times of the on-site printing process. As a general recommendation, it is in any case advisable to try to protect

doi:10.20944/preprints202112.0357.v2

the printing site as much as possible from thermal excursions, in order to limit the variability of the compressive strengths in the building.

5 Conclusions

This paper is part of the research on 3D printing of earthen housing modules, made with soil taken in situ. Previous studies have already led to the definition of 3D printed earthen elements for the external cladding of single-story wooden load-bearing structures. With this work, we intended to take a step forward in the use of 3D printed earthen elements, studying their load-bearing capacity for vertical loads. The compressive strength of the 3D printed earthen elements turned out to be comparable to the compressive strength of traditional rammed earth buildings.

Since the ultimate goal of this line of research is to build load-bearing structures entirely in earth, consisting of two or more floors, the present work investigated two of the major alleged criticalities of 3D printed multi-story earthen buildings: detachments due to poor cohesion between extruded layers and detachments between internal infill and external shell. The uniaxial compression test did not actually show any particular danger for the stability of the structure, due to detachment phenomena. Rather, the experimental results showed some mechanical behaviors that were completely unexpected, as quite anomalous for a brittle construction material. Among these, the most important are the almost zero value of (apparent) Poisson's ratio in the elastic regime and the contractive behavior until the end of the test. The causes of these two anomalous behaviors have different origins, rheological for the first and structural for the second. In fact, the contractive behavior (at the mesoscale) is the result of a poor propagation of cracks, due to the crack stopper action of the infill. This means that the infill of the 3D printed elements has not only a filling function, but a real structural function.

The crack stopper action of the infill is then the cause of several other anomalous behaviors of the 3D printed elements made with earthen mixtures, such as high values of resistant area of the cross-section and low values of Poisson's ratio until the end of the uniaxial compression test.

Supplementary Materials: The following are available online at www.mdpi.com/xxx/s1, Figure S1: The Gaia House by WASP: first prototype of a 3D printed earthen building with biodegradable materials (built in 2018) [source WASP], Figure S2: The Tecla House by WASP: 3D printing of the second prototype of an earthen building (completed in 2021) [source WASP], Figure S3: Experimental laws of the normalized resistant area, A_{res}/A_n, and of the damage parameter, D_2, for variable slenderness of a cylindrical concrete specimen (uniaxial compression test), Figure S4: Interpolating law of the average unloading-reloading slope, for variable slenderness of a cylindrical concrete specimen (uniaxial compression test), Figure S5: Failure mechanism of a cylindrical concrete specimen (uniaxial compression test), Figure S6: Ratio of the transverse strain, ε_r, to the longitudinal strain, ε_l, with the transverse strain acquired both on the external surface and inside the resistant structure (concrete specimen in uniaxial compression), Figure S7: Acquisition of the transverse strain, Figure S8: The values of ε_ϑ, with the transverse strain acquired both on the external surface and inside the resistant structure (concrete specimen in uniaxial compression), Figure S9: Stress/strain curves for variable slenderness of a cylindrical concrete specimen (uniaxial compression test), Table S1: Description of the components of the LT mix.

Author Contributions: Conceptualization, M.M.; methodology, E.F., M.M., A.C., L.N., F. De F. and M.V.; software, E.F., M.M., A.C., L.N., F. De F. and M.V.; validation, E.F.; formal analysis, E.F.; investigation, E.F.; resources, E.F., M.M., A.C., L.N., F. De F. and M.V.; data curation, E.F.; writing—original draft preparation, E.F.; writing—review and editing, M.M., A.C., L.N., F. De F. and M.V.; visualization, E.F.; supervision, E.F., M.M., A.C., L.N., F. De F. and M.V.; project administration, M.M. All authors have read and agreed to the published version of the manuscript.

Funding: This research received no external funding.

Acknowledgments: The authors wish to thank RiceHouse s.r.l. (Andorno Micca (BI), Italy, website: www.ricehouse.it) for the supply of rice husk and the technical advice.

Conflicts of Interest: The authors declare no conflict of interest.

References

1. Aubert, J.E.; Maillard, P.; Morel, J.-C.; Al Rafii, M. Towards a simple compressive strength test for earth bricks? *Mater. Struct.* **2016**, *49(5)*, 1641–1654.
2. Azeredo, G.; Morel, J.-C.; Lamarque, C.-H. Applicability of rheometers to characterizing earth mortar behavior. Part I: experimental device and validation. *Mater. Struct*. **2008**, *41*, 1465–1472.
3. Bui, Q.-B.; Morel, J.-C.; Hans, S.; Meunier, N. Compression behaviour of nonindustrial materials in civil engineering by three scale experiments: the case of rammed earth. *Mater. Struct*. **2009**, *42*, 1101–1116.
4. Moevus, M.; Jorand, Y.; Olagnon, C.; Maximilien, S.; Anger, R.; Fontaine, L.; Arnaud, L. Earthen construction: an increase of the mechanical strength by optimizing the dispersion of the binder phase, *Mater. Struct*. **2015**, *49(4)*, 1–14.
5. Deboucha, S.; Hashim, R. A review on bricks and stabilized compressed earth blocks. *Scientific Research and Essays* **2011**, *6(3)*, 499–506.
6. Pacheco-Torgal, F. Jalali, S. Earth construction: lessons from the past for future eco-efficient construction. *Constr. Build. Mater.* **2012**, *29(April)*, 512–519.
7. Treloar, G.; Owen, C.M.; Fay, M.R. Enviromental assessment of rammed earth construction systems. *Structural Survey* **2001**, *19 (2)*, 99–105.
8. Keefe, L. *Earth Building Methods and Materials, repair and conservation*; Taylor & Francis: London, New York, 2005.
9. Gallipoli, D.; Bruno, A.W.; Perlot, C.; Salmon, N. *Raw earth construction: is there a role for unsaturated soil mechanics*; Taylor & Francis Group: London, UK, 2014.
10. Schroeder, H. *Sustainable Building with Earth*; Springer International Publishing, 2016.
11. Perrot, A.; Rangeard, D.; Courteille, E. 3D printing of earth-based materials: Processing aspects. *Constr. Build. Mater*. **2018**, *172*, 670–676.
12. Bruno, A.W.; Gallipoli, D.; Perlot, C.; Mendes, J. Effect of stabilisation on mechanical properties, moisture buffering and water durability of hypercompacted earth. *Constr. Build. Mater*. **2017**, *149*, 733–740.
13. Khelifi, H.; Perrot, A.; Lecompte, T.; Ausias, G. Design of clay/cement mixtures for extruded building products. *Mater. Struct.* **2013**, *46*, 999–1010.
14. Maskell, D.; Heath, A.; Walker, P. Laboratory scale testing of extruded earth masonry units. *Mater. Des*. **2013**, *45*, 359–364.
15. Ouellet-Plamondon, C.M.; Habert, G. Self-Compacted Clay based Concrete (SCCC): proof-of-concept. *J. Clean Prod*. **2016**, *117*, 160–168.
16. Perrot, A.; Rangeard, D.; Pierre, A. Structural built-up of cement-based materials used for 3D- printing extrusion techniques. *Mater. Struct*. **2016**, *49*, 1213–1220.
17. Wangler, T.; Lloret, E.; Reiter, L.; Hack, N.; Gramazio, F.; Kohler, M.; Bernhard, M.; Dillenburger, B.; Buchli, J.; Roussel, N.; Flatt, R. Digital Concrete: Opportunities and Challenges. *RILEM Tech. Lett*. **2016**, *1*, 67–75.
18. Houben, H.; Guillaud, H. *Earth construction: a comprehensive guide*; Intermediate Technology Publications: London, UK, 1994.
19. Nagaraj, H.B.; Rajesh, A.; Sravan, M.V. Influence of soil gradation, proportion and combination of admixtures on the properties and durability of CSEBs. *Constr. Build. Mater*. **2016**, *110*, 135–144.
20. Fitzmaurice, R. *Manual on stabilized soil construction for housing*; Technical Assistance Programme, United Nations: New York City, New York Country, 1958.
21. Reddy, B.; Jagadish, KS. Influence of soil composition on the strength and durability of soil-cement blocks. *Indian Concrete Journal* **1995**, *69(9)*, 517–524.
22. Reddy, B.; Kumar, P.P. Role of clay content and moisture on characteristics of cement stabilised rammed earth. Proceedings of the 11th International Conference on Non- Conventional Materials and Technologies (NOCMAT). Bath University, U.K, 6-9 September 2009; iisc: Bath, UK.
23. Walker, P.; Stace, T. Properties of some cement stabilised compressed earth blocks and mortars. *Mater. Struct*. **1997**, *30(203)*, 545–551.
24. Bryan, A.J. Criteria for the suitability of soil for cement stabilization. *Build. Environ*. **1988**, *23(4)*, 309–319.
25. Ciancio, D.; Boulter, M. Stabilised rammed earth: a case study in Western Australia. *Proceedings of the Institution of Civil Engineers - Engineering Sustainability* **2012**, *165(2)*, 141–154.
26. Reddy, B.; Jagadish, K.S. Properties of soil–cement block masonry. *Masonry International* **1989**, *3(2)*, 80–84.
27. Spence, R.J.S. Predicting the performance of soil-cement as a building material in tropical countries. *Build. Sci*. **1975**. *10*, 155.
28. Webb, D. Stabilised soil and the built environment. *Renewable Energy* **1994**, *5(5–8)*, 1066–1080.
29. Readle, D.; Coghlan, S.; Smith, J.C.; Corbin, A.; Augarde, C.E. Fibre reinforcement in earthen construction materials. *Proc. Inst. Civ. Eng. Constr. Mater*. **2016**, *169(5)*, 252–260.
30. Walker, P. Editorial. *Proc. Inst. Civ. Eng. Constr. Mater.* **2017**, *170(1)*, 1–2.
31. Yang, F.; Zhang, B.; Ma, Q. Study of sticky rice− lime mortar technology for the restoration of historical masonry construction. *Acc. Chem. Res*. **2010**, *43(6)*, 936–944.
32. Maskell, D.; Heath, A.; Walker, P. Comparing the Environmental Impact of Stabilisers for Unfired Earth Construction. *Key Eng. Mater.* **2014**, *600*, 132–143.
33. Plank, J. Applications of biopolymers and other biotechnological products in building materials. *Appl. Microbiol. Biotechnol*. **2004**, *66(1)*, 1–9.

34. Serraiocco, L.D.; Barbero, D.; Maroni, A.; Peyrot, S. Effects of lime-stabilization of A-4 Soils in its Monotonic Strength and Deformation parameters for Road Use. *Journal of Geotechnical Engineering (JoGE)* **2021**, *8(1)*, 12–23.
35. Barbero, D.; Serraiocco, L.D.; Maroni, A.; Peyrot, S. Portland Cement for A-4 Group Soils Stabilization. *Journal of Geotechnical Engineering (JoGE)* **2021**, *8(1)*, 41–49.
36. Muguda Viswanath, S. Biopolymer Stabilised Earthen Construction Materials. PhD thesis, Durham University, UK, 2019.
37. Gallipoli, D.; Bruno, A.W.; Perlot, C.; Mendes, J. A geotechnical perspective of raw earth building. *Acta Geotech*. **2017**, *12(3)*, 463–478.
38. Lax, C. Life cycle assessment of rammed earth. Master thesis, University of Bath, UK, 2010.
39. Reddy, B.; Kumar, P.P. Embodied energy in cement stabilised rammed earth walls. *Energy Build*. **2010**, *42(3)*, 380–385.
40. Fujita, Y.; Ferris, F.G.; Lawson, R.D.; Colwell, F.S.; Smith, R.W. Subscribed content calcium carbonate precipitation by ureolytic subsurface bacteria. *Geomicrobiol. J*. **2000**, *17(4)*, 305–318.
41. Ivanov, V.; Stabnikov, V. *Construction Biotechnology: Biogeochemistry, Microbiology and Biotechnology of Construction Materials and Processes*; Springer: Singapore, 2016.
42. Renforth, P.; Manning, D.A.C.; Lopez-Capel, E. Carbonate precipitation in artificial soils as a sink for atmospheric carbon dioxide. *Appl. Geochem*. **2009**, *24(9)*, 1757–1764.
43. Cabalar, A.F.; Canakci, H. Direct shear tests on sand treated with xanthan gum. *Proc. Inst. Civ. Eng. Ground Improv*. **2011**, *164*, 57–64.
44. Chang, I.; Im, J.; Prasidhi, A.K.; Cho, G.-C. Effects of Xanthan gum biopolymer on soil strengthening. *Constr. Build. Mater*. **2015**, *74(10)*, 65–72.
45. Chen, C.; Wu, L.; Perdjon, M.; Huang, X.; Peng, Y. The drying effect on xanthan gum biopolymer treated sandy soil shear strength. *Constr. Build. Mater*. **2019**, *197*, 271–279.
46. Chang, I.; Prasidhi, A.K.; Im, J.; Cho, G.-C. Soil strengthening using thermo-gelation biopolymers. *Constr. Build. Mater*. **2015**, *77*, 430–438.
47. Ayeldeen, M.K.; Negm, A.M.; El Sawwaf, M.A. Evaluating the physical characteristics of biopolymer/soil mixtures. *Arabian J. Geosci*. **2016**, *9(5)*, 329–339.
48. Nakamatsu, J.; Kim, S.; Ayarza, J.; Ramírez, E.; Elgegren, M.; Aguilar, R. Eco-friendly modification of earthen construction with carrageenan: Water durability and mechanical assessment. *Constr. Build. Mater*. **2017**, *139*, 193–202.
49. Aguilar, R.; Nakamatsu, J.; Ramírez, E.; Elgegren, M.; Ayarza, J.; Kim, S.; Pando, M.A.; Ortega-San-Martin, L. The potential use of chitosan as a biopolymer additive for enhanced mechanical properties and water resistance of earthen construction. *Constr. Build. Mater*. **2016**, *114*, 625–637.
50. Pacheco-Torgal, F.; Ivanov, V.; Karak, N.; Jonkers, H. *Biopolymers and Biotech Admixtures for Eco-Efficient Construction Materials*; Woodhead Publishing: 2016.
51. Chang, I.; Im, J.; Cho, G.-C. Introduction of Microbial Biopolymers in Soil Treatment for Future Environmentally-Friendly and Sustainable Geotechnical Engineering. *Sustainability* **2016**, *8(3)*, 251.
52. Chen, R.; Zhang, L.; Budhu, M. Biopolymer Stabilization of Mine Tailings. *J. Geotech. Geoenviron. Eng*. **2013**, *139(October)*, 130128212232006.
53. Latifi, N.; Horpibulsuk, S.; Meehan, C.L.; Abd Majid, M.Z.; Tahir, M.M.; Mohamad, E.T. Improvement of Problematic Soils with Biopolymer—An Environmentally Friendly Soil Stabilizer. *J. Mater. Civ. Eng*. **2017**, *29(2)*.
54. Qureshi, M.U.; Chang, I.; Al-Sadarani, K. Strength and durability characteristics of biopolymer-treated desert sand. *Geomech. Eng*. **2017**, *12(5)*, 785–801.
55. Siddique, R.; Singh, K.; Kunal, M.; Corinaldesi Singh, V.; Rajor, A. Properties of bacterial rice husk ash concrete. *Constr. Build. Mater*. **2016**, *121*, 112–119.
56. Singh, B. Rice husk ash. In *Waste and supplementary cementitious materials in concrete*; Elsevier: 2018; pp. 417-460.
57. Moretti, M.; Chiusoli, A.; Naldoni, L.; De Fabritiis, F.; Visonà, M. Earthen 3d printed constructions towards a new high-efficient way of building. In *Past and present of the earthen architectures in China and Italy*; Luvidi, L., Fratini, F., Rescic, S., Zhang, J., Eds.; Cnr Edizioni: Roma, Italy, 2021; pp. 147–155.
58. Ferretti, E.; Moretti, M.; Chiusoli, A.; Naldoni, L.; De Fabritiis, F.; Visonà, M. Rice Husk Shredding as a Means of Increasing the Long-Term Mechanical Properties of Earthen Mixtures for 3D Printing. *Materials*, submitted.
59. Colombo, D. Tecla, la casa stampata in 3D in terra cruda. *3Dprinting Creative* **2021**, April.
60. Vincenzini, A.; Augarde, C.E.; Gioffrè, M. Experimental characterization of natural fibre–soil interaction: lessons for earthen construction. *Mater. Struct*. **2021**, *54*, 110.
61. Viswanath, S.M.; Booth, S.J.; Hughes, P.N.; Augarde, C.E.; Perlot, C.; Bruno, A.W.; Gallipoli, D. Mechanical properties of biopolymer-stabilised soil-based construction materials. *Géotechnique Letters* **2017**, *7(4)*, 1–18.
62. Alhumayani, H.; Gomaa, M.; Soebarto, V.; Jabi, W. Environmental assessment of large-scale 3D printing in construction: A comparative study between cob and concrete. *J. Cleaner Prod*. **2020**, *270*, 122463.
63. Gomaa, M.; Jabi, W.; Veliz Reyes, A.; Soebarto, V. 3D printing system for earth-based construction: Case study of cob. *Autom. Constr*. **2021**, *124*, 103577.
64. Lecompte, T.; Perrot, A. Non-linear modeling of yield stress increase due to SCC structural build-up at rest. *Cem. Concr. Res*. **2017**, *92*, 92–97.
65. Lootens, D.; Jousset, P.; Martinie, L.; Roussel, N.; Flatt, R.J. Yield stress during setting of cement pastes from penetration tests. *Cem. Concr. Res*. **2009**, *39*, 401–408.

---

66. Mettler, L.K.; Wittel, F.K.; Flatt, R.J.; Herrmann, H.J. Evolution of strength and failure of SCC during early hydration. *Cem. Concr. Res*. **2016**, *89*, 288–296.
67. Roussel, N. A thixotropy model for fresh fluid concretes: theory, validation and applications. *Cem. Concr. Res*. **2006**, *36*, 1797–1806.
68. Highway Research Board – Bulletin 65. *Mapping and Subsurface Exploration for Engineering Purposes*. National Academy of Sciences – National Research Council, publication 252: Washington, D. C.: 1952.
69. UNI EN ISO 14688-1:2018. Geotechnical investigation and testing - Identification and classification of soil - Part 1: Identification and description; 2018 (March).
70. Barbero, D.; Boano, P.; Colla, M.T.; Forno, M.G. Pleistocene terraced fluvial succession, northern slope of Torino Hill. *Quat. Int*. **2007**, *171–172*, 64–71.
71. Khoshnevis, B. Automated Construction by Contour Crafting—Related Robotics and Information Technologies, *Journal of Automation in Construction – Special Issues: The best of ISARC 2002* **2004**, *13(1)*, 5–19.
72. Khoshnevis, B.; Hwang, D.; Yao, K.-T.; Yeh, Z. Mega-Scale Fabrication by Contour Crafting, *Int. J. Ind. Syst. Eng*. **2006**, *1*, 301–320.
73. Technical Notes on Brick Construction. *Specifications and classification of Brick*; Brick Industry Association: Reston, Virginia, 2007 (October, 9A).
74. ASTM C652-21. *Standard Specification for Hollow Brick (Hollow Masonry Units Made From Clay or Shale)*; 2021 (June).
75. Gowthaman, S.; Iki, T.; Nakashima, K.; Ebina, K.;·Kawasaki, S. Feasibility study for slope soil stabilization by microbial induced carbonate precipitation (MICP) using indigenous bacteria isolated from cold subarctic region. *SN Applied Sciences* **2019**, *1*, 1480.
76. Proudfoot, D.; Brooks, L.; Gammons, C.H.; Barth , E.; Bless, D.; Nagisetty, R.M.; Lauchnor, E.G. Investigating the potential for microbially induced carbonate precipitation to treat mine waste. *J. Hazard. Mater*. **2022**, 424, 127490.
77. Imran, M.A.; Kimura, S.; Nakashima, K.; Evelpidou, N.; Kawasaki, S. Feasibility Study of Native Ureolytic Bacteria for Biocementation Towards Coastal Erosion Protection by MICP Method. *Appl. Sci*. **2019**, *9*, 4462.
78. Hudson, J.A.; Brown, E.T.; Fairhurst, C. Optimizing the control of rock failure in servo-controlled laboratory tests. *Rock. Mech*. **1971**, *3*, 217–224. doi:10.1007/BF01238181.
79. Ferretti, E. On Strain-softening in dynamics. *Int. J. Fract.Mech*. **2004**, *126(4)*, L75–L82.
80. Ferretti, E. Shape-effect in the effective laws of plain and rubberized concrete. *CMC-Comput. Mater. Continua* **2012**, *30(3)*, 237–284.
81. Ferretti, E. A discussion of strain-softening in concrete. *Int. J. Fract*. **2004**, *126(1)*, L3–L10.
82. Rinde, J. A. Poisson's ratio for rigid plastic foams. *J. Appl. Polym. Sci*. **2003**, *14(8)*,1913–1926.
83. Ferretti, E. On Poisson's ratio and volumetric strain in concrete. *Int. J. Fract*. **2004**, *126(3)*, L49–L55.
84. Wu, M.X.; Du, B.; Yao, Y.C.; He X.F.. An experimental study on stress-strain behavior and constitutive model of hardfill material. *Science China Physics, Mechanics & Astronomy* **2011**, *54(11)*, 2015–2024.
85. Ostrowsky, J. A New Approach for Evaluating the Ductility, Volumetric Stiffness, and Permeability of Cutoff Wall Backfill Materials. Graduate Thesis, Utah State University, Logan, Utah (USA), 2019.
86. Bažant, Z.P.; Belytschko, T.B.; Chang, T.-P. Continuum Theory for Strain-Softening. *J. Eng. Mech*. **1984**, 110(12), 1666–1692.
87. Soldo, A.; Miletic, M.; Aguilar, V. Macroscopic stress-strain response and strain localization behavior of biopolymer-treated soil. *Research Square* **2021**, preprint.
88. Ferretti, E. On nonlocality and locality: Differential and discrete formulations. Proceedings of the 11th International Conference on Fracture 2005 – ICF11, Turin, Italy, 20-25 March 2005; International Congress on Fracture (ICF) - Curran Associates, Inc.: New York, USA, 2010; Volume 3, pp. 1728–1733.
89. Ferretti, E.; Di Leo, A.; Viola, E. A novel approach for the identification of material elastic constants. In CISM Courses and Lectures - Problems in Structural Identification and Diagnostics: General Aspects and Applications, Proceedings of the Workshop on Problems in Structural Identification and Diagnostics, Bologna, Italy, 15-16 July 2002; Davini, C., Viola, E., Eds.; Springer-Verlag: Vienna, Austria, 2003; Volume 471, pp. 117–131.